

elasticity is conceptually simpler to develop with the Lagrangian description, and this is the framework we shall almost always adopt. Note that a seismogram is the record of motion of a particular part of the Earth (namely, the particles to which the seismometer was attached during installation), so it is directly a record of Lagrangian motion.

We shall work in this chapter with a Cartesian coordinate system (x_1, x_2, x_3) , and all tensors here are Cartesian tensors. We use the term *displacement*, regarded as a function of space and time, and written as $\mathbf{u} = \mathbf{u}(\mathbf{x}, t)$, to denote the vector distance of a particle at time t from the position \mathbf{x} that it occupies at some reference time t_0 , often taken as $t = 0$. Since \mathbf{x} does not change with time, it follows that the *particle velocity* is $\partial\mathbf{u}/\partial t$ and that the *particle acceleration* is $\partial^2\mathbf{u}/\partial t^2$.

To analyze the distortion of a medium, whether it be solid or fluid, elastic or inelastic, we use the *strain tensor*. If a particle initially at position \mathbf{x} is moved to position $\mathbf{x} + \mathbf{u}$, then the relation $\mathbf{u} = \mathbf{u}(\mathbf{x})$ is used to describe the displacement field. To examine the distortion of the part of the medium that was initially in the vicinity of \mathbf{x} , we need to know the new position of the particle that was initially at $\mathbf{x} + \delta\mathbf{x}$. This new position is $\mathbf{x} + \delta\mathbf{x} + \mathbf{u}(\mathbf{x} + \delta\mathbf{x})$. Any distortion is liable to change the relative position of the ends of the line-element $\delta\mathbf{x}$. If this change is $\delta\mathbf{u}$, then $\delta\mathbf{x} + \delta\mathbf{u}$ is the new vector line-element, and by writing down the difference between its end points we obtain

$$\delta\mathbf{x} + \delta\mathbf{u} = \mathbf{x} + \delta\mathbf{x} + \mathbf{u}(\mathbf{x} + \delta\mathbf{x}) - (\mathbf{x} + \mathbf{u}(\mathbf{x})).$$

Since $|\delta\mathbf{x}|$ is arbitrarily small, we can expand $\mathbf{u}(\mathbf{x} + \delta\mathbf{x})$ as $\mathbf{u} + (\delta\mathbf{x} \cdot \nabla)\mathbf{u}$ plus negligible terms of order $|\delta\mathbf{x}|^2$. It follows that $\delta\mathbf{u}$ is related to gradients of \mathbf{u} and to the original line-element $\delta\mathbf{x}$ via

$$\delta\mathbf{u} = (\delta\mathbf{x} \cdot \nabla)\mathbf{u}, \quad \text{or} \quad \delta u_i = \frac{\partial u_i}{\partial x_j} \delta x_j. \quad (2.1)$$

However, we do not need all of the nine independent components of the tensor $u_{i,j}$ to specify true distortion in the vicinity of \mathbf{x} , since part of the motion is due merely to an infinitesimal rigid-body rotation of the neighborhood of \mathbf{x} . This can be seen from the identity $(u_{i,j} - u_{j,i})\delta x_j = \varepsilon_{ijk}\varepsilon_{jlm}u_{m,l}\delta x_k$ (see Box 2.2 and Problem 2.2), so that equation (2.1) can be rewritten as

$$\delta u_i = \frac{1}{2}(u_{i,j} + u_{j,i})\delta x_j + \frac{1}{2}(\text{curl } \mathbf{u} \times \delta\mathbf{x})_i, \quad (2.2)$$

and the rigid-body rotation is of amount $\frac{1}{2}\text{curl } \mathbf{u}$. The interpretation of the last term in (2.2) as a rigid-body rotation is valid if $|u_{i,j}| \ll 1$. If displacement gradients were not “infinitesimal” in the sense of this inequality, then we should instead have to analyze the contribution to $\delta\mathbf{u}$ from a *finite* rotation—a much more difficult matter, since finite rotations do not commute and cannot be expressed as vectors.

In terms of the infinitesimal strain tensor, defined to have components

$$e_{ij} \equiv \frac{1}{2}(u_{i,j} + u_{j,i}), \quad (2.3)$$

contributions due to the traction $\mathbf{T}(\mathbf{u}, \mathbf{n})$ and to the displacement \mathbf{u} itself on S . However, the way in which each of these three contributions is weighted is unsatisfactory, since each involves a Green function with source at \mathbf{x} and observation point at ξ . (Note that the last term in (2.41) involves differentiation with respect to ξ_l .) We want \mathbf{x} to be the observation point, so that the total displacement obtained there can be regarded as the sum (integral) of contributing displacements at \mathbf{x} due to each volume element and surface element. The reciprocal theorem for \mathbf{G} must be invoked, but this will require extra conditions on Green's function itself, since the equation $G_{in}(\xi, t - \tau; \mathbf{x}, 0) = G_{ni}(\mathbf{x}, t - \tau; \xi, 0)$ (see (2.39)) was proved only if \mathbf{G} satisfies homogeneous boundary conditions on S , whereas (2.41) is valid for *any* Green function set up by an impulsive force in the n -direction at $\xi = \mathbf{x}$ and $\tau = t$.

We shall examine two different cases. Suppose, first, that Green's function is determined with S as a rigid boundary. We write $\mathbf{G}^{\text{rigid}}$ for this function and $G_{in}^{\text{rigid}}(\xi, t - \tau; \mathbf{x}, 0) = 0$ for ξ in S . Then (2.41) becomes

$$\begin{aligned} u_n(\mathbf{x}, t) &= \int_{-\infty}^{\infty} d\tau \iiint_V f_i(\xi, \tau) G_{ni}^{\text{rigid}}(\mathbf{x}, t - \tau; \xi, 0) dV \\ &\quad - \int_{-\infty}^{\infty} d\tau \iint_S u_i(\xi, \tau) c_{ijkl} n_j \frac{\partial}{\partial \xi_l} G_{nk}^{\text{rigid}}(\mathbf{x}, t - \tau; \xi, 0) dS. \end{aligned} \quad (2.42)$$

Alternatively, we can use \mathbf{G}^{free} as Green's function, so that the traction $c_{ijkl} n_j (\partial/\partial \xi_l) G_{kn}^{\text{free}}(\xi, t - \tau; \mathbf{x}, 0)$ is zero for ξ in S , finding

$$\begin{aligned} u_n(\mathbf{x}, t) &= \int_{-\infty}^{\infty} d\tau \iiint_V f_i(\xi, \tau) G_{in}^{\text{free}}(\mathbf{x}, t - \tau; \xi, 0) dV \\ &\quad + \int_{-\infty}^{\infty} d\tau \iint_S G_{ni}^{\text{free}}(\mathbf{x}, t - \tau; \xi, 0) T_i(\mathbf{u}(\xi, \tau), \mathbf{n}) dS. \end{aligned} \quad (2.43)$$

Equations (2.41)–(2.43) are all different forms of the representation theorem and each has its special uses. Taken together, they seem to imply a contradiction to the question of whether $\mathbf{u}(\mathbf{x}, t)$ depends upon displacement on S (see (2.42)) or traction (see (2.43)) or both (see (2.41)). But since traction and displacement cannot be specified independently on the surface of an elastic medium, there is no contradiction. In (2.41), the Green function is not completely defined.

The surface on which values of traction (or displacement) are explicitly required has been taken, in this chapter, as external to the volume V . It is often useful instead to take this surface to include two adjacent internal surfaces, being the opposite faces of a buried fault. Specialized forms of the representation theorem can then be developed, which enable one to analyze the earthquakes set up by activity on a buried fault. This subject is central to earthquake source theory, taken up in Chapter 3 and developed much further in Chapters 10 and 11.

So far, we have considered only Cartesian coordinate systems. In practice, the seismologist is often required to use non-Cartesian coordinates that allow the physical relationship between components of displacement, stress, and strain to be simplified for the geometry

At first sight, it is somewhat surprising that our spatially concentrated body force (proportional to $\delta(\mathbf{x})$) has potentials (4.17) that are nonzero outside the source region. This often happens in elasticity, and it brings out the artificiality of the potential method.

The second step in finding displacements is to solve wave equations for the Lamé potentials ϕ and ψ . From (4.5), (4.13), and (4.17), we get

$$\ddot{\phi} = -\frac{X_0(t)}{4\pi\rho} \frac{\partial}{\partial x_1} \frac{1}{|\mathbf{x}|} + \alpha^2 \nabla^2 \phi \quad (4.18)$$

and

$$\ddot{\psi} = \frac{X_0(t)}{4\pi\rho} \left(0, \frac{\partial}{\partial x_3} \frac{1}{|\mathbf{x}|}, -\frac{\partial}{\partial x_2} \frac{1}{|\mathbf{x}|} \right) + \beta^2 \nabla^2 \psi. \quad (4.19)$$

The solution of (4.18) follows by comparison with (4.5) and (4.6), so that here

$$\phi(\mathbf{x}, t) = -\frac{1}{(4\pi\alpha)^2\rho} \iiint_V \frac{X_0\left(t - \frac{|\mathbf{x} - \boldsymbol{\xi}|}{\alpha}\right)}{|\mathbf{x} - \boldsymbol{\xi}|} \frac{\partial}{\partial \xi_1} \frac{1}{|\boldsymbol{\xi}|} dV(\boldsymbol{\xi}). \quad (4.20)$$

Fortunately, this integral can be simplified by integrating over the volume V via the system of concentric spherical shells centered on \mathbf{x} . If $\alpha\tau$ is the radius of a typical shell S , so that $|\mathbf{x} - \boldsymbol{\xi}| = \alpha\tau$ and the shell thickness is $\alpha d\tau$, then

$$\phi(\mathbf{x}, t) = -\frac{1}{(4\pi\alpha)^2\rho} \int_0^\infty \frac{X_0(t - \tau)}{\tau} \left(\iint_S \frac{\partial}{\partial \xi_1} \frac{1}{|\boldsymbol{\xi}|} dS \right) d\tau.$$

In Box 4.3, it is shown that the integral over S is a simple explicit function of \mathbf{x} and τ , and it follows that

$$\phi(\mathbf{x}, t) = -\frac{1}{4\pi\rho} \left(\frac{\partial}{\partial x_1} \frac{1}{|\mathbf{x}|} \right) \int_0^{|\mathbf{x}|/\alpha} \tau X_0(t - \tau) d\tau. \quad (4.21)$$

Similarly, for the vector Lamé potential, one finds

$$\psi(\mathbf{x}, t) = \frac{1}{4\pi\rho} \left(0, \frac{\partial}{\partial x_3} \frac{1}{|\mathbf{x}|}, -\frac{\partial}{\partial x_2} \frac{1}{|\mathbf{x}|} \right) \int_0^{|\mathbf{x}|/\beta} \tau X_0(t - \tau) d\tau. \quad (4.22)$$

The third and final step in obtaining the displacement due to body force $X_0(t)$ applied in the x_1 -direction at the origin is to form $\nabla\phi + \nabla \times \psi$ from (4.21) and (4.22). Using $r = |\mathbf{x}|$, this gives

$$\begin{aligned} u_i(\mathbf{x}, t) &= \frac{1}{4\pi\rho} \left(\frac{\partial^2}{\partial x_i \partial x_1} \frac{1}{r} \right) \int_{r/\alpha}^{r/\beta} \tau X_0(t - \tau) d\tau \\ &\quad + \frac{1}{4\pi\rho\alpha^2 r} \left(\frac{\partial r}{\partial x_i} \frac{\partial r}{\partial x_1} \right) X_0\left(t - \frac{r}{\alpha}\right) + \frac{1}{4\pi\rho\beta^2 r} \left(\delta_{i1} - \frac{\partial r}{\partial x_i} \frac{\partial r}{\partial x_1} \right) X_0\left(t - \frac{r}{\beta}\right). \end{aligned}$$

4.2.1 PROPERTIES OF THE FAR-FIELD P -WAVE

We introduce here the *far-field P -wave*, which for (4.23) has the displacement \mathbf{u}^P given by

$$u_i^P(\mathbf{x}, t) = \frac{1}{4\pi\rho\alpha^2} \gamma_i \gamma_j \frac{1}{r} X_0 \left(t - \frac{r}{\alpha} \right). \quad (4.24)$$

As in (4.23), this is for a point force $X_0(t)$ in the x_j -direction at the origin. Along a given direction $\boldsymbol{\gamma}$ from the source, it follows from (4.24) that this wave

- (i) attenuates as r^{-1} ;
- (ii) has a waveform that depends on the time–space combination $t - r/\alpha$, and therefore propagates with speed α (recall that $\alpha^2 = (\lambda + 2\mu)/\rho$);
- (iii) has a displacement waveform that is proportional to the applied force at retarded time; and
- (iv) has a direction of displacement at \mathbf{x} that is parallel to the direction $\boldsymbol{\gamma}$ from the source. This follows from the property $u_i^P \propto \gamma_i$ (see (4.24)). The far-field P -wave is therefore *longitudinal* (sometimes called *radial*) in that its direction of particle motion is the same as the direction of propagation. If $t = 0$ is chosen as the time at which $X_0(t)$ first becomes nonzero, then r/α is the *arrival time* of the P -wave at r .

4.2.2 PROPERTIES OF THE FAR-FIELD S -WAVE

The *far-field S -wave* in (4.23) has displacement \mathbf{u}^S given by

$$u_i^S(x, t) = \frac{1}{4\pi\rho\beta^2} (\delta_{ij} - \gamma_i \gamma_j) \frac{1}{r} X_0 \left(t - \frac{r}{\beta} \right). \quad (4.25)$$

As in (4.23), this is for a point force $X_0(t)$ in the x_j -direction at the origin. Recall that $\boldsymbol{\gamma}$ is the unit vector directed from the source to the receiver. Along a given direction $\boldsymbol{\gamma}$, this wave

- (i) attenuates as r^{-1} ;
- (ii) propagates with speed β and has arrival time r/β at \mathbf{x} ;
- (iii) has a displacement waveform that is proportional to the applied force at retarded time; and
- (iv) has a direction of displacement \mathbf{u}^S at \mathbf{x} that is perpendicular to the direction $\boldsymbol{\gamma}$ from the source. (From (4.25) it is easy to show that $\mathbf{u}^S \cdot \boldsymbol{\gamma} = 0$.) The far-field S -wave is therefore a *transverse* wave, because its direction of particle motion is normal to the direction of propagation.

Radiation patterns for \mathbf{u}^P and \mathbf{u}^S are given in Figure 4.2.

4.2.3 PROPERTIES OF THE NEAR-FIELD TERM

We define the near-field displacement \mathbf{u}^N in (4.23) by

Since $\boldsymbol{\gamma}$ is a unit vector at the source, directed along the ray to \mathbf{x} , the problem of obtaining the radiation pattern of the P -wave is simply a matter of expressing $\boldsymbol{\gamma} \cdot \boldsymbol{\nu}$ and $\boldsymbol{\gamma} \cdot \dot{\bar{\mathbf{u}}}$ in terms of strike ϕ_s , dip δ , rake λ , take-off angle i_ξ , and source–receiver azimuth ϕ . The radiation patterns for SV and SH are slightly more complicated because the separation into SV and SH is not immediately apparent in (4.85). Clearly, this formula does indicate that \mathbf{u}^S is a transverse motion, because $\mathbf{u}^S \cdot \boldsymbol{\gamma} = 0$. It follows that SV and SH motions, which are (respectively) in the directions $\hat{\mathbf{p}}$ and $\hat{\boldsymbol{\phi}}$ of Figure 4.10, are given by

$$\mathbf{u}^{SV}(\mathbf{x}, t) = (\mathbf{u}^S \cdot \hat{\mathbf{p}}) \hat{\mathbf{p}} = \frac{[(\boldsymbol{\gamma} \cdot \boldsymbol{\nu})(\dot{\bar{\mathbf{u}}} \cdot \hat{\mathbf{p}}) + (\boldsymbol{\gamma} \cdot \dot{\bar{\mathbf{u}}})(\boldsymbol{\nu} \cdot \hat{\mathbf{p}})]\mu A \hat{\mathbf{p}}}{4\pi\rho\beta^3 r} \quad (4.86)$$

and

$$\mathbf{u}^{SH}(\mathbf{x}, t) = (\mathbf{u}^S \cdot \hat{\boldsymbol{\phi}}) \hat{\boldsymbol{\phi}} = \frac{[(\boldsymbol{\gamma} \cdot \boldsymbol{\nu})(\dot{\bar{\mathbf{u}}} \cdot \hat{\boldsymbol{\phi}}) + (\boldsymbol{\gamma} \cdot \dot{\bar{\mathbf{u}}})(\boldsymbol{\nu} \cdot \hat{\boldsymbol{\phi}})]\mu A \hat{\boldsymbol{\phi}}}{4\pi\rho\beta^3 r}. \quad (4.87)$$

To obtain all three radiation patterns in terms of $(\phi_s, \delta, \lambda, i_\xi, \phi)$, we introduce Cartesian coordinate directions $\hat{\mathbf{x}}, \hat{\mathbf{y}}, \hat{\mathbf{z}}$ at the epicenter. Our choice is $\hat{\mathbf{x}}$ = North, $\hat{\mathbf{y}}$ = East, and $\hat{\mathbf{z}}$ = vertically downward, as shown in Figure 4.20. In terms of these three unit vectors,

$$\begin{aligned} \text{slip } \bar{\mathbf{u}} &= \bar{u} (\cos \lambda \cos \phi_s + \cos \delta \sin \lambda \sin \phi_s) \hat{\mathbf{x}} \\ &\quad + \bar{u} (\cos \lambda \sin \phi_s - \cos \delta \sin \lambda \cos \phi_s) \hat{\mathbf{y}} \\ &\quad - \bar{u} \sin \lambda \sin \delta \hat{\mathbf{z}}, \\ \text{fault normal } \boldsymbol{\nu} &= -\sin \delta \sin \phi_s \hat{\mathbf{x}} + \sin \delta \cos \phi_s \hat{\mathbf{y}} - \cos \delta \hat{\mathbf{z}}, \\ P\text{-wave direction } \mathbf{l} = \boldsymbol{\gamma} &= \sin i_\xi \cos \phi \hat{\mathbf{x}} + \sin i_\xi \sin \phi \hat{\mathbf{y}} + \cos i_\xi \hat{\mathbf{z}}, \\ SV\text{-wave direction } \hat{\mathbf{p}} &= \cos i_\xi \cos \phi \hat{\mathbf{x}} + \cos i_\xi \sin \phi \hat{\mathbf{y}} - \sin i_\xi \hat{\mathbf{z}}, \\ SH\text{-wave direction } \hat{\boldsymbol{\phi}} &= -\sin \phi \hat{\mathbf{x}} + \cos \phi \hat{\mathbf{y}}. \end{aligned} \quad (4.88)$$

Six different scalar products are needed in the radiation pattern formulas (4.84), (4.86), (4.87), and these can readily be obtained from (4.88). In dimensionless form, the radiation patterns \mathcal{F}^P , \mathcal{F}^{SV} , and \mathcal{F}^{SH} are given by

$$\begin{aligned} \mathcal{F}^P &= 2(\boldsymbol{\gamma} \cdot \boldsymbol{\nu})(\boldsymbol{\gamma} \cdot \dot{\bar{\mathbf{u}}}) / \dot{\bar{u}} \\ &= \cos \lambda \sin \delta \sin^2 i_\xi \sin 2(\phi - \phi_s) - \cos \lambda \cos \delta \sin 2i_\xi \cos(\phi - \phi_s) \\ &\quad + \sin \lambda \sin 2\delta (\cos^2 i_\xi - \sin^2 i_\xi \sin^2(\phi - \phi_s)) \\ &\quad + \sin \lambda \cos 2\delta \sin 2i_\xi \sin(\phi - \phi_s), \end{aligned} \quad (4.89)$$

$$\begin{aligned}
\dot{S}\dot{P} &= -2\rho_1 \frac{\cos j_1}{\beta_1} G p \beta_1 / (\alpha_2 D), \\
\dot{S}\dot{S} &= 2\rho_1 \frac{\cos j_1}{\beta_1} E \beta_1 / (\beta_2 D), \\
\dot{P}\dot{P} &= 2\rho_2 \frac{\cos i_2}{\alpha_2} F \alpha_2 / (\alpha_1 D), \\
\dot{P}\dot{S} &= -2\rho_2 \frac{\cos i_2}{\alpha_2} G p \alpha_2 / (\beta_1 D), \\
\dot{P}\dot{P} &= - \left[\left(b \frac{\cos i_1}{\alpha_1} - c \frac{\cos i_2}{\alpha_2} \right) F + \left(a + d \frac{\cos i_2}{\alpha_2} \frac{\cos j_1}{\beta_1} \right) G p^2 \right] / D, \\
\dot{P}\dot{S} &= 2 \frac{\cos i_2}{\alpha_2} \left(a c + b d \frac{\cos i_1}{\alpha_1} \frac{\cos j_1}{\beta_1} \right) p \alpha_2 / (\beta_2 D), \\
\dot{S}\dot{P} &= 2\rho_2 \frac{\cos j_2}{\beta_2} H p \beta_2 / (\alpha_1 D), \\
\dot{S}\dot{S} &= 2\rho_2 \frac{\cos j_2}{\beta_2} E \beta_2 / (\beta_1 D), \\
\dot{S}\dot{P} &= 2 \frac{\cos j_2}{\beta_2} \left(a c + b d \frac{\cos i_1}{\alpha_1} \frac{\cos j_1}{\beta_1} \right) p \beta_2 / (\alpha_2 D), \\
\dot{S}\dot{S} &= \left[\left(b \frac{\cos j_1}{\beta_1} - c \frac{\cos j_2}{\beta_2} \right) E + \left(a + d \frac{\cos i_1}{\alpha_1} \frac{\cos j_2}{\beta_2} \right) H p^2 \right] / D. \quad (5.40)
\end{aligned}$$

For two different solids that meet at a planar interface, but are not in welded contact, then traction is still continuous but by implication sliding can take place. Chaisri and Krebes (2000) consider displacement discontinuities on $z = 0$ such that

$$\begin{aligned}
\tau_{zx1} &= \tau_{zx2}, & u_{x2} - u_{x1} &= c_x \tau_{zx}, \\
\tau_{zz1} &= \tau_{zz2}, & u_{z2} - u_{z1} &= c_z \tau_{zz},
\end{aligned} \quad (5.41)$$

where c_x and c_z are constants and subscripts 1 and 2 refer to the upper and lower media. They obtained 16 coefficients of the same general form as (5.40). But in their more general case (i.e., with c_x and c_z not equal to zero), there is an explicit dependence on frequency, absent in (5.40).

5.2.5 ENERGY FLUX

For a steady-state plane wave incident on the boundary between two homogeneous half-spaces, there is no possibility of trapping energy at the interface (otherwise amplitudes

apparent, together with minor contributions from a leaking mode (another type of interface wave).

At the outset, we must emphasize that the best way to solve Lamb's problem is via Laplace transformation and the inversion methods of Cagniard. The discussion of integration paths in the complex ray-parameter plane is then relatively simple; and the actual inversion of the Laplace transform, to obtain pulse shapes in the time domain, is made trivial. A self-contained description of these methods is given here in Sections 6.4 and 6.5. We introduce this material, however, with a Fourier transform. In part, this is an acknowledgment to the vast literature on the subject, including books by Ewing *et al.* (1957), Brekhovskikh (1960), and Červený and Ravindra (1971), and many hundreds of papers. But the major reason for developing Fourier-transform methods in connection with Lamb's problem is to prepare the ground for Chapter 9, which gives practical methods for calculating seismograms in realistic structures. We shall find there that the reflectivity method for layered media and powerful solution methods for problems of grazing incidence are based on numerical work with the Fourier transform rather than analytic inversion of the Laplace transform.

6.1 Spherical Waves as a Superposition of Plane Waves and Conical Waves

Consider an inhomogeneous wave equation with source at the origin and time dependence $\exp(-i\omega t)$:

$$\frac{\partial^2 \phi}{\partial t^2} - c^2 \nabla^2 \phi = 4\pi c^2 \delta(\mathbf{x}) \exp(-i\omega t). \quad (6.1)$$

The solution of this equation (in an infinite homogeneous space) is obtained from (4.4) as

$$\phi(\mathbf{x}, t) = \frac{1}{R} \exp \left[i\omega \left(\frac{R}{c} - t \right) \right], \quad (6.2)$$

where $R = \sqrt{x^2 + y^2 + z^2}$.

Equation (6.1) can also be solved by recognizing the time dependence of $\phi(\mathbf{x}, t)$ as the steady oscillation $\exp(-i\omega t)$ and then using Fourier-transform methods to derive the spatial dependence. From transformation of (6.1) we find that

$$\phi(\mathbf{k}, t) = [4\pi c^2 / (k^2 c^2 - \omega^2)] \exp(-i\omega t),$$

where $k^2 = k_x^2 + k_y^2 + k_z^2$. Then from (6.2) and the triple inverse transform of $\phi(\mathbf{k}, t)$,

$$\frac{1}{R} \exp \left[i\omega \left(\frac{R}{c} - t \right) \right] = \frac{\exp(-i\omega t)}{2\pi^2} \iiint_{-\infty}^{\infty} \frac{\exp(i\mathbf{k} \cdot \mathbf{x})}{k^2 - \frac{\omega^2}{c^2}} dk_x dk_y dk_z. \quad (6.3)$$

The left-hand side of (6.3) is a spherical wave propagating from the origin with speed c . Its amplitude is a function only of radial distance and has no directional variation. The right-hand side of (6.3) is a superposition of plane waves $\exp[i(\mathbf{k} \cdot \mathbf{x} - \omega t)]$ over the entire range of k_x, k_y, k_z , weighted by $[2\pi^2(k^2 - \omega^2/c^2)]^{-1}$. It therefore appears that we have

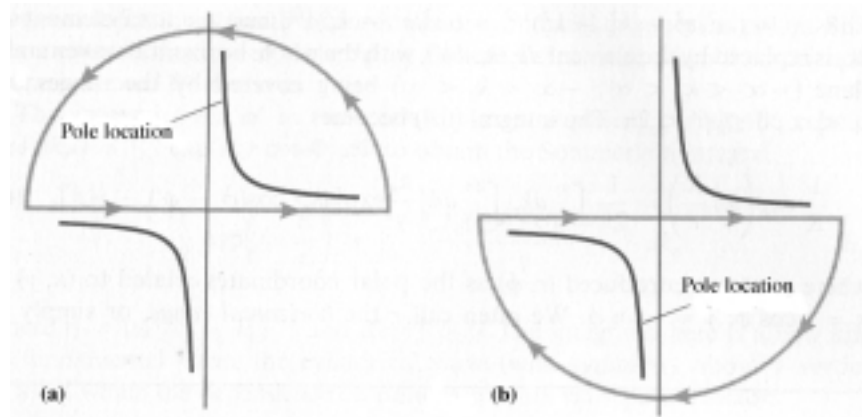


FIGURE 6.2

Paths of integration in the complex k_z -plane for obtaining the Weyl integral. (a) The path when $z > 0$. (b) $z < 0$.

The residue evaluation is now straightforward. For $z > 0$ the factor $\exp(ik_z z)$ suppresses the integrand in (6.3) if it is taken around a sufficiently large semicircle in the upper half-plane (see Fig. 6.2a). Adding this semicircle to the integration path along the real axis, we have a closed path going in the positive direction around a pole at $k_z = i\gamma$ in the first quadrant, so that

$$\phi = 2\pi i \times \text{residue} = \frac{\exp(-i\omega t)}{2\pi} \iint_{-\infty}^{\infty} \frac{\exp(ik_x x + ik_y y - \gamma z)}{\gamma} dk_x dk_y.$$

For $z < 0$, we add a sufficiently large semicircle in the lower half-plane (Fig. 6.2b) to obtain a closed path in the negative (i.e., clockwise) direction, which picks up a pole at $k_z = -i\gamma$ in the third quadrant:

$$\phi = -2\pi i \times \text{residue} = \frac{\exp(-i\omega t)}{2\pi} \iint_{-\infty}^{\infty} \frac{\exp(ik_x x + ik_y y + \gamma z)}{\gamma} dk_x dk_y.$$

Combining these results for $z > 0$ and $z < 0$, we obtain the Weyl integral

$$\frac{1}{R} \exp\left(i\omega \frac{R}{c}\right) = \frac{1}{2\pi} \iint_{-\infty}^{\infty} \frac{\exp(ik_x x + ik_y y - \gamma|z|)}{\gamma} dk_x dk_y, \quad (6.4)$$

where $\gamma = \sqrt{k_x^2 + k_y^2 - \omega^2/c^2}$ and the sign of γ is chosen so that $\text{Re } \gamma > 0$. In the limiting case of zero attenuation, this becomes $\text{Re } \gamma \geq 0$.

In the above expression, the plane waves in the integrand do satisfy the wave equation with velocity c , so that the spherical wave is indeed represented by a superposition of such plane waves. Note that for some parts of the (k_x, k_y) integration, the plane waves are inhomogeneous. This occurs for $\omega^2/c^2 < k_x^2 + k_y^2$, so that γ becomes positive real

FIGURE 6.12

Diagrams for interpretation of the generalized reflection for a point source in an elastic half-space. (a) The source–receiver geometry and a reflected P -wave defining the reflection angle i_s . (b) Branch cuts for ξ and η in the complex p -plane, together with a pole at $p = 1/c_R$. (Note: For attenuating media, the branch cuts and pole on the positive real axis move up into the first quadrant.) (c) The steepest descents path Γ for the exponent in (6.33), this being the path such that $pr + \xi z + \xi h = R_0/\alpha +$ positive imaginary quantity $= R_0/\alpha + iX^2$. One may solve for p to find

$$R_0^2 p = r(iX^2 + R_0/\alpha) \pm \sqrt{X^4 - 2iX^2 R_0/\alpha (z + h)}$$

on Γ , crossing the real axis at $p = p_s = \alpha^{-1} \sin i_s$ and also at $p = 1/(\alpha \sin i_s)$. (d) For small i_s , the steepest descents path can be taken (going on to the sheet $\text{Im } \xi < 0, \text{Im } \eta < 0$ in the first quadrant, as in Fig. 6.8). (e) For large i_s , the integration path (wholly on the top Riemann sheet) can be thought of as a sum of two branch-cut integrals, Γ_α and Γ_β , plus a circuit Γ_R picking up the residue from the Rayleigh pole.

BOX 6.7*Outstanding features of Rayleigh waves from a buried point source*

1. Attenuation behaves like $r^{-1/2}$ with distance, as compared with body waves ($\sim r^{-1}$) and head waves (r^{-2}), so that Rayleigh waves must dominate the ground motion at sufficient range. Note that the ratio between horizontal and vertical motions in the cylindrical Rayleigh wave (6.37) is just that found for a plane Rayleigh wave in Problem 5.4b.
2. Phase delay is given by $\omega r/c_R$, and is independent of depth h , so that the travel time curve is a straight line.
3. Amplitude is an exponentially decaying function of h and ω :

$$\exp[-\omega \sqrt{c_R^{-2} - \alpha^{-2}} h] \sim \exp[-\sqrt{0.9} \omega h / \beta].$$

For an S -wave source, this becomes

$$\exp[-\omega \sqrt{c_R^{-2} - \beta^{-2}} h] \sim \exp[-\sqrt{0.2} \omega h / \beta].$$

4. Particle motion is retrograde elliptical (w has a phase shift of $-\pi/2$ with respect to u , and hence a phase advance of $+\pi/2$; see Box 5.5), and the ellipticity is the same as for the free Rayleigh waves described in Section 5.3.
5. From items 2 and 3 above, the slope of the phase spectrum is a function of range but not of depth, and the shape of the amplitude spectrum is a function of depth but not of range. Therefore, the amplitude and phase are independent of each other. This is a common feature of what we generally call *normal modes*, to be investigated in more detail for a layered medium in Chapter 7. This independence, of course, violates causality (see Box 5.8), hence it is meaningless to speak of the “first motion” of Rayleigh waves or individual normal modes.

that is,

$$p = \begin{cases} \frac{xt - |z + z_0| \sqrt{\frac{R_0^2}{\beta_1^2} - t^2}}{R_0^2} & t \leq \frac{R_0}{\beta_1} \\ \frac{xt + i|z + z_0| \sqrt{t^2 - \frac{R_0^2}{\beta_1^2}}}{R_0^2} & t \geq \frac{R_0}{\beta_1} \end{cases} \quad (6.57a)$$

$$p = \begin{cases} \frac{xt - |z + z_0| \sqrt{\frac{R_0^2}{\beta_1^2} - t^2}}{R_0^2} & t \leq \frac{R_0}{\beta_1} \\ \frac{xt + i|z + z_0| \sqrt{t^2 - \frac{R_0^2}{\beta_1^2}}}{R_0^2} & t \geq \frac{R_0}{\beta_1} \end{cases} \quad (6.57b)$$

where $R_0 = \sqrt{x^2 + (z + z_0)^2}$ is the distance between receiver and image source (see Fig. 6.15b). It is interesting to compare this Cagniard path with the steepest descents path of integration for (6.56). To find this latter path, we adopt the terminology of Box 6.3 with $x = s$, $\zeta = p$, and $f = -(px + \eta_1|z + z_0|)$. A saddle point $p = p_s$ must be such that $f'(p_s) = 0$, i.e., $x \cos j_s = |z + z_0| \sin j_s$, where $p_s = \beta_1^{-1} \sin j_s$, so that p_s is just the ray parameter for the reflected ray between source and receiver, having j_s as the angle of incidence in the upper medium (Fig. 6.15a). Note that some close parallels with Section 6.2 are beginning to emerge (see (6.19)). In that section, we analyzed a P -wave problem, used a Fourier transform, and considered a point source. Yet here we find essentially the same saddle-point position. A difference now is that the steepest descents path is perpendicular to the real p -axis; i.e., angle $\chi = \pi/2$ (see Box 6.3), whereas previously we found $\chi = -\pi/4$. In fact, where the Cagniard path lies on the real axis (6.57a), it lies on a “ridge” of the integrand, the ridge descending to a saddle point at $p_s = x/(R_0\beta_1) = \beta_1^{-1} \sin j_s$ as t increases to R_0/β_1 . There the Cagniard path turns through $\pi/2$ and follows a “valley” of the integrand, which is the ordinary steepest descents path for t increasing from R_0/β_1 (see (6.57b)).

If the receiver is in a position such that $x/R_0 < \beta_1/\beta_2$, then the point of departure of the Cagniard path from the real p -axis lies to the left of branch cuts emanating from $p = 1/\beta_1$ and $p = 1/\beta_2$. (The inequality implies that x is less than the critical distance at which head waves begin to be observable.) No interference with the branch cuts can occur, and since

$$dp/dt = i\eta_1/\sqrt{t^2 - R_0^2/\beta_1^2} \quad \text{on } C \text{ (for } t > R_0/\beta_1),$$

it follows that

$$v^{\text{refl}}(x, z, t) = \frac{A}{2\pi\rho_1\beta_1^2} \operatorname{Re} \left\{ \frac{\mu_1\eta_1 - \mu_2\eta_2}{\mu_1\eta_1 + \mu_2\eta_2} \right\} \frac{H(t - R_0/\beta_1)}{\sqrt{t^2 - R_0^2/\beta_1^2}}. \quad (6.58)$$

(There is no contribution for $t < R_0/\beta_1$, since then $p(t)$ is real (see (6.57a)), and the integrand (6.56) has zero imaginary part.) This algebraic formula (6.58) is exact, and is evaluated for $t > R_0/\beta_1$ by first using (6.57b) to obtain a corresponding point on the Cagniard path, then finding $\eta_i = \sqrt{\beta_i^{-2} - p^2}$ ($i = 1, 2$); and finally, substituting into (6.58). This is an example of what we can naturally call a *narrow-angle* reflection.

If the receiver is beyond the critical distance, so that $\beta_1/\beta_2 < x/R_0 < 1$ and we expect a *wide-angle* reflection (see discussion of (6.23)), then the Cagniard path departs from the real p -axis at a point $p = p_s$ between $1/\beta_2$ and $1/\beta_1$, as shown in Figure 6.15b. The

deformation from the positive imaginary p -axis (6.56) to the Cagniard path proceeds just as before, but now there can be a contribution from that part of the path which lies on the real p -axis. This is the head-wave contribution, which arises in the evaluation of (6.56) along the Cagniard path for real p -values between $1/\beta_2$ and $\beta_1^{-1} \sin j_s$; then η_2 is pure imaginary, so that the integrand has a nonzero imaginary part. Corresponding values of time are found from (6.57):

$$\text{at } p = 1/\beta_2, \quad t = t_h = x/\beta_2 + |z + z_0| \sqrt{\beta_1^{-2} - \beta_2^{-2}},$$

t_h being the arrival time at (x, z) of head waves from $(0, z_0)$;

$$\text{at } p = \beta_1^{-1} \sin j_s, \quad t = R_0/\beta_1,$$

the arrival time of the wide-angle reflection. Between times t_h and R_0/β_1 , η_2 is a negative pure imaginary quantity. It follows that an exact formula for the generalized reflection is

$$\begin{aligned} v^{\text{refl}}(x, z, t) = & \frac{A}{2\pi\rho_1\beta_1^2} \operatorname{Im} \left\{ \frac{\mu_1\eta_1 - \mu_2\eta_2}{\mu_1\eta_1 + \mu_2\eta_2} \right\} \frac{H(t - t_h) - H(t - R_0/\beta_1)}{\sqrt{R_0^2/\beta_1^2 - t^2}} \\ & + \frac{A}{2\pi\rho_1\beta_1^2} \operatorname{Re} \left\{ \frac{\mu_1\eta_1 - \mu_2\eta_2}{\mu_1\eta_1 + \mu_2\eta_2} \right\} \frac{H(t - R_0/\beta_1)}{\sqrt{t^2 - R_0^2/\beta_1^2}}. \end{aligned} \quad (6.59)$$

The last term here evaluates the shape of the wide-angle reflection at time $t > R_0/\beta_1$. However, there is a phase shift, because associated waves in the lower medium are inhomogeneous ($p > 1/\beta_2$). As we showed in Box 5.6 and in Section 6.2, the pulse shape of the wide-angle reflection is a linear sum of the incident pulse shape and its Hilbert transform. The latter involves motions often called the head-wave term. In this sense, one can speak of the wide-angle reflection as “emerging from the tail of the head wave.” Note, however, that the attempt to separate the head-wave and reflection contributions will fail whenever there is a breakdown of the approximate (asymptotic) theory for each contribution (e.g., (6.26), if the receiver is near the critical distance, so that L is very small). Although this is a breakdown of terminology, (6.59) continues to give the exact total effect of “head wave” plus “reflection” even when L is small.

The final problem we shall consider in this section on the exact impulse response for two-dimensional problems is that of a line source of P – SV waves in a half-space taken as the region $z < 0$, with a free surface at $z = 0$ so that a Rayleigh wave is generated. We closely follow Chapman (1972), obtaining exact results that have many points of similarity with Section 6.3 above. One new idea is introduced: the concept of a “leaking mode,” associated with zeros of the Rayleigh function lying in the Riemann sheet $\{\operatorname{Re} \xi < 0; \operatorname{Re} \eta > 0\}$.

We shall consider P – SV motions with displacement only in the x - and z -directions. Then, from an argument given in Section 5.1, it is sufficient to work with scalar potentials ϕ and ψ related to displacement via

$$\mathbf{u} = \nabla\phi + \nabla \times (0, \psi, 0) = (\partial\phi/\partial x - \partial\psi/\partial z, 0, \partial\phi/\partial z + \partial\psi/\partial x). \quad (6.60)$$

$$\chi(\mathbf{x}, s) = \frac{N_0}{2\pi^2 \rho \beta^2} \int_0^\infty dq \operatorname{Im} \left[\int_0^{i\infty} \frac{\exp(-s(pr + \eta|z|))}{\eta} dp \right], \quad (6.82)$$

where $\eta = \sqrt{\beta^{-2} + q^2 - p^2}$. (To obtain (6.82) from (6.81), we also used half-ranges of integration and properties of evenness in q ; and evenness and oddness in w for the real and imaginary parts of the integrand.)

Strong similarities are now apparent between the integrands of (6.48) and (6.82). Note here that the horizontal variable is r , rather than x , and $1/\beta^2 + q^2$ replaces $1/\beta^2$ in the definition of η . Previously, we found that

$$\operatorname{Im} \left[\int_0^{i\infty} \frac{\exp(-s(px + \eta|z|))}{\eta} dp \right] \quad \left(\text{with } \eta = \sqrt{\beta^{-2} - p^2} \right)$$

is the Laplace transform of

$$\frac{H\left(t - \frac{\sqrt{x^2 + z^2}}{\beta}\right)}{\sqrt{t^2 - \frac{x^2 + z^2}{\beta^2}}},$$

and this enables us now to write (6.82) as

$$\chi(\mathbf{x}, s) = \frac{N_0}{2\pi^2 \rho \beta^2} \int_0^\infty dq \int_0^\infty \frac{H[t - R\sqrt{\beta^{-2} + q^2}]}{\sqrt{t^2 - R^2(\beta^{-2} + q^2)}} e^{-st} dt. \quad (6.83)$$

Here we are using $R = \sqrt{x^2 + y^2 + z^2} = \sqrt{r^2 + z^2}$ as the three-dimensional distance function. If we integrate with respect to q first, and then with respect to t , we find

$$\chi(\mathbf{x}, s) = \frac{N_0}{2\pi^2 \rho \beta^2} \int_0^\infty dt e^{-st} \left\{ H\left(t - \frac{R}{\beta}\right) \int_0^{\sqrt{t^2/R^2 - 1/\beta^2}} \frac{dq}{\sqrt{t^2 - R^2(\beta^{-2} + q^2)}} \right\} \quad (6.84)$$

(as explained in Fig. 6.20). But now from this integrand we can recognize the required solution as

$$\chi(\mathbf{x}, t) = \frac{N_0}{2\pi^2 \rho \beta^2} H\left(t - \frac{R}{\beta}\right) \int_0^{\sqrt{t^2/R^2 - 1/\beta^2}} \frac{dq}{\sqrt{t^2 - R^2(\beta^{-2} + q^2)}}. \quad (6.85)$$

This is essentially the method of de Hoop (1960), and we list the following comments on (6.85):

- (i) The solution has the typical form for point-source problems, in that the exact solution is a single finite integral.

Then it is an elementary exercise in convolutions to show that

$$\chi(\mathbf{x}, t) = \frac{d\psi}{dt} * \frac{1}{\sqrt{t}} * \frac{1}{\pi\sqrt{t}} = \psi(t),$$

and in this sense we can actually get a useful *algebraic* expression for the seismogram, given by (6.95).

The approximation (6.94) and the resulting convolution (6.96) are now very much a part of modern seismology, as we shall find in Chapter 9 when looking at the effects of multiple layering.

6.6 Summary of Main Results and Comparison between Different Methods

We have described two methods for solving problems of a spherical wave interacting with a plane boundary. The first method (Sections 6.1–6.3) uses the Fourier transform of time dependence, and leads to solutions for displacement, pressure, etc. as a function of frequency. The second method (Sections 6.4–6.5) uses a Laplace transform, but (by manipulations due to Cagniard, de Hoop, and others) leads to solutions directly in the time domain. In this section we list some similarities and differences between the two methods and briefly discuss their merits and disadvantages.

First, we list the similarities. Both the Fourier method and the Cagniard method entail integrations in the complex ray-parameter plane: ray paths in the physical problem correspond to saddle points in the integrand under consideration; head waves correspond to branch cuts; interface waves (e.g., Rayleigh, Stoneley) correspond to poles; and leaking modes (e.g., \bar{P}) correspond to poles on Riemann sheets other than that on which the radiation condition is satisfied.

Second, there are several superficial differences. (i) To obtain results in the time domain via the Fourier method, a numerical inverse transform is required. But, in practice, the Cagniard solution must be convolved with a source function and with the instrument response, and these operations are essentially equivalent to numerical Fourier transformations. (ii) We characterized the Cagniard methods as being exact, whereas early in the development of the Fourier method, we made an approximation to certain Hankel functions (see (6.16)–(6.18)). In practice, an equivalent approximation (6.94) is often made in the Cagniard approach. (iii) Branch cuts in the Cagniard method were chosen to make $\{\text{Re } \xi \geq 0; \text{Re } \eta \geq 0\}$, and it was found possible to keep the path of integration on this same physical Riemann sheet, without crossing branch cuts. However, we developed the Fourier theory with branch cuts fixed by $\{\text{Im } \xi \geq 0; \text{Im } \eta \geq 0\}$, in which case we found it necessary to develop complicated paths of integration (e.g., Fig. 6.9) that had segments on non-physical sheets. Many authors have taken this approach, and a correct discussion of the effect of leaking modes can be highly involved. Fortunately, the choice of branch cuts is quite flexible in the Fourier method, and a path of integration can in fact be chosen that does lie close to the steepest descents path, yet also stays on the same Riemann sheet. The main constraint, the radiation condition, requires that the integrand (e.g., (6.33)) tend to zero as $|z| \rightarrow 0$ only for values of p on the original path of integration. Thus, in (6.33), we really require $\text{Im } \xi \geq 0$ only for p -values on the real p -axis, and do *not* need to use branch cuts

FIGURE 6.22 (continued)

Various branch cuts and integration paths in the complex p -plane, showing the flexibility of choice. (a)–(d) are relevant to the problem solved in Section 6.2 of a point source of pressure in a medium consisting of two fluid half-spaces. (a) Branch cuts are chosen so that $\text{Im } \xi_1 > 0$, $\text{Im } \xi_2 > 0$ for the whole plane. Γ lies on the real axis, just above cuts in the third quadrant, and below cuts in the first. Compare with Figure 6.4. (b) For the same problem, we have changed branch cuts to $\text{Re } \xi_1 > 0$, $\text{Re } \xi_2 > 0$. The solution is unchanged, because Γ is unchanged and the value of an integrand (e.g., (6.18)) at any point on Γ is unchanged from (a). (c) Γ is distorted from the position shown in (b) to lie on a steepest descents path in a case where head waves are possible. The path around the cut is now much simpler than that shown in Figure 6.9, although there is still a problem in that the steepest descents path runs into the cuts at $p = 1/(\alpha_1 \sin i_s)$, hence Γ is subsequently drawn below the cut. (d) For cuts like those shown here, there is no difficulty in keeping Γ everywhere on the steepest descents path (except around the branch point at $p = 1/\alpha_2$). To see that these cuts are possible, note that they can be moved from the position shown in (a) before Γ is distorted from the real axis. In subsequent distortion of Γ to the path shown here, $\text{Im } \xi_1$ and $\text{Im } \xi_2$ do become negative in the first quadrant to the left of the cuts shown. This is allowed because no singularities are present between this part of Γ and a path (shown as a broken line) on which $\text{Im } \xi_1$ and $\text{Im } \xi_2$ are positive. (e) This shows the p -plane for a solid half-space problem, e.g., for evaluating the generalized $\dot{P}\dot{P}$ reflection (see Fig. 6.12 for comparison). Branch cuts are drawn upward into the first quadrant, and a path Γ favorable for computations is made up from straight-line segments and a semicircle around $p = 1/c_R$. Branch cuts of this type have properties similar to the lines of poles found in Chapter 9 in generating theoretical seismograms when the Earth's spherical geometry is taken into account.

Gilbert, F., and L. Knopoff. The directivity problem for a buried line source. *Geophysics*, **26**, 626–634, 1961.

Johnson, L. R. Green's function for Lamb's problem. *Geophysical Journal of the Royal Astronomical Society*, **37**, 99–131, 1974.

Lamb, H. On the propagation of tremors over the surface of an elastic solid. *Philosophical Transactions of the Royal Society of London*, **A203**, 1–42, 1904.

Lapwood, E. R. The disturbance due to a line source in a semi-infinite elastic medium. *Philosophical Transactions of the Royal Society of London*, **A242**, 63–100, 1949.

Pekeris, C. L. The seismic buried pulse. *Proceedings of the National Academy of Sciences*, **41**, 629–639, 1955.

Richards, P. G. Elementary solutions to Lamb's problem for a point source and their relevance to three-dimensional studies of spontaneous crack propagation. *Bulletin of the Seismological Society of America*, **69**, 947–956, 1979.

Verweij, M. D. Reflection of transient acoustic waves by a continuously layered halfspace with depth-dependent attenuation. *Journal of Computational Acoustics*, **5**, 265–276, 1997.

Wilson, C. R. The Abel-Fourier method of Hankel transformation: Applications to seismic data. *Geophysical Prospecting*, **34**, 545–568, 1986.

Problems

- 6.1 When head waves can occur in the solution (6.93), arriving at time t_h , show that (6.94) is equivalent to requiring

$$\frac{r}{\beta_2} \gg t - t_h.$$

BOX 7.2 (continued)

Let us now use these values of c and U to analyse the seismogram at a particular distance $x = 500$ km, assuming it is given by

$$f(500, t) = \frac{1}{2\pi} \int_{-\infty}^{\infty} \exp [i(k500 - \omega t)] d\omega. \quad (1)$$

This assumes a unit amplitude spectrum, and all frequencies leave the source at $x = 0$ with the same zero initial phase.

art/r107bf02c.eps

The phase of (1) at seven different times, giving examples where ω_s has 0, 1, or 2 values.

Figure C shows the phase of (1), plotted as a function of ω at 20 s increments from $t = 80$ to 200 s. It can be seen that the phase at times $t = 80$ and 200 s does not have stationary values—that is, there is no solution of $d(kx - \omega t)/d\omega = 0$ for $(x, t) = (500, 80)$ or $(500, 200)$. For $t = 100, 120,$ and 160 s there is only one stationary value, a solution ω_s of equation (7.14). And for $t = 180$ s, there are two solutions ω_s .

- 7.3 Generalize the idea expressed in the previous question by relating both $\mathbf{f}(z_l)$ and $\mathbf{f}(z_{l-1})$ to \mathbf{w}_l and then showing that

$$\mathbf{f}(z_l) = \mathbf{F}_l(z_l) \mathbf{F}_l^{-1}(z_{l-1}) \mathbf{f}(z_{l-1}).$$

Hence show that the propagator from z_0 to z_k is

$$\mathbf{P}(z_k, z_0) = \left[\mathbf{F}_k(z_k) \mathbf{F}_k^{-1}(z_{k-1}) \right] \left[\mathbf{F}_{k-1}(z_{k-1}) \mathbf{F}_{k-1}^{-1}(z_{k-2}) \right] \cdots \left[\mathbf{F}_1(z_1) \mathbf{F}_1^{-1}(z_0) \right].$$

(Note: These results are still true if the medium consists of a stack of inhomogeneous layers, provided $\mathbf{F}_l(z)$ is a matrix whose columns are linearly independent solutions of $\partial \mathbf{f} / \partial z = \mathbf{A}(z) \mathbf{f}$ in the l th layer.)

- 7.4 In Sections 5.4 and 7.2, we showed that $\mathbf{F} \mathbf{w}$ can be thought of as a sum of all the possible wave types that solve $\partial \mathbf{f} / \partial z = \mathbf{A} \mathbf{f}$; that each of the columns of \mathbf{F} is separately a basic solution of $\partial \mathbf{f} / \partial z = \mathbf{A} \mathbf{f}$; and that \mathbf{w} is a vector of constants that give the weight of each basic solution present in the sum $\mathbf{F} \mathbf{w}$. Consider the first column of \mathbf{F} in (7.55) when $k > \omega / \alpha$, and show that the corresponding wave in the sum $\mathbf{F} \mathbf{w}$ of (7.54) is an inhomogeneous P -wave with displacement amplitude

$$\dot{P} e^{-\gamma z} \sqrt{\alpha^2 k^2 / \omega^2 - \sin^2(kx - \omega t)}.$$

- 7.5 Show by redefining the origin that one way to construct $G_{np}(0, 0, h; x, y, z; \omega)$ is by making the switches ($r \rightarrow r; \phi \rightarrow \phi + \pi; z \rightarrow h; h \rightarrow z$) in formulas for $G_{np}(x, y, z; 0, 0, h; \omega)$. Use this approach to verify that the reciprocity

$$G_{np}(0, 0, h; x, y, z; \omega) = G_{pn}(x, y, z; 0, 0, h; \omega)$$

is satisfied for surface-wave components (7.146) and (7.147).

- 7.6 Show that the change in phase velocity of Love waves at fixed wavenumber, which will result from a perturbation ($\delta \rho, \delta \mu$) in the structure, is

$$\left(\frac{\delta c}{c} \right)_k = \frac{\int_0^\infty \left[k^2 l_1^2 + \left(\frac{dl_1}{dz} \right)^2 \right] \delta \mu dz - \int_0^\infty \omega^2 l_1^2 \delta \rho dz}{2\omega^2 \int_0^\infty \rho l_1^2 dz}.$$

- 7.7 Show that the Rayleigh-wave eigenfunction for a half-space with Poisson's ratio 0.25 is given by

$$\begin{aligned} r_1 &= e^{-0.8475kz} - 0.5773 e^{-0.3933kz}, \\ r_2 &= 0.8475 e^{-0.8475kz} - 1.4679 e^{-0.3933kz}, \end{aligned}$$

and that the energy integral I_1 is equal to $0.6205\rho/k$ (k is the horizontal wavenumber and ρ is the density). Then, using (7.150), obtain an explicit formula for

BOX 8.1 (continued)

stopping at either x or 1 (times a constant) as the last term. The first few Legendre polynomials are

$$P_0(x) = 1, \quad P_1(x) = x, \quad P_2 = \frac{1}{2}(3x^2 - 1),$$

$$P_3(x) = \frac{1}{2}(5x^3 - 3x), \quad P_4(x) = \frac{1}{8}(35x^4 - 30x^2 + 3),$$

and, in general,

$$P_l(x) = \frac{1}{2^l l!} \frac{d^l}{dx^l} (x^2 - 1)^l,$$

which is known as *Rodrigues' formula*.

The figure shows some examples of Legendre functions, plotted as (large scale, axially symmetric) topography on a sphere. $P_l(\cos \Delta)$ has l oscillations around the circumference. Note from the figure (e.g., with $l = 5, 10, 14$) that these oscillations are not quite evenly spaced: there is an increase in wavelength and amplitude for the peaks (or troughs) at $\Delta = 0$ and $\Delta = \pi$.

art/r108bf01.eps

THE CASES $m \neq 0$

We shall initially assume the integer m is positive. Then with $x = \cos \Delta$ in (3), we find

$$\frac{d}{dx} \left[(1 - x^2) \frac{d\Theta}{dx} \right] = \frac{m^2 \Theta}{1 - x^2} - K \Theta. \quad (11)$$

We might attempt a power-series solution like (5). However, this approach becomes difficult because the formula for b_{i+2} turns out to involve not just b_i (as it did before for Θ)

(continued)

integral such as $\int_V {}_i \mathbf{u}^*(\boldsymbol{\xi}) \cdot \mathbf{f}(\boldsymbol{\xi}) dV(\boldsymbol{\xi})$, where $\mathbf{f}(\boldsymbol{\xi})$ is now the body force per unit volume. We shall continue to assume that this body force acts as a step function in time. From (8.25) we immediately obtain

$$\mathbf{u}(\mathbf{x}, t) = \sum_i \left(\int_V {}_i \mathbf{u}^*(\boldsymbol{\xi}) \cdot \mathbf{f}(\boldsymbol{\xi}) dV \right) {}_i \mathbf{u}(\mathbf{x}) \frac{1 - \exp[-(\omega_i t / 2Q_i)] \cos \omega_i t}{\omega_i^2}. \quad (8.26)$$

Our use of i here denotes the i th normal mode of the whole Earth. That is, each i corresponds to some value for the triplet of integers (l, m, n) that we found in Section 8.1 were necessary for characterizing individual modes. The sum in (8.25) is thus an infinite sum, but, as shown by Rayleigh in his classic text “The Theory of Sound” (reprinted 1945, paragraph 101), it does converge because of the factor ω_i^{-2} . The normal modes in (8.26) have been normalized (cf. (8.18)) by

$$\int_V \rho(\boldsymbol{\xi}) {}_j \mathbf{u}^*(\boldsymbol{\xi}) \cdot {}_i \mathbf{u}(\boldsymbol{\xi}) dV = \delta_{ij}, \quad (8.27)$$

where $\rho(\boldsymbol{\xi})$ is the density, and the volume integrals above are taken over the whole Earth.

We shall now find the vibration of a spherical Earth model due to a point source that is specified by a moment tensor. Using a result that was previously given as an exercise (Problem 3.6), the body force becomes

$$f_p(\boldsymbol{\xi}, t) = -M_{pq}(t) \frac{\partial}{\partial \xi_q} \delta(\boldsymbol{\xi} - \mathbf{x}_s). \quad (8.28)$$

We shall assume that \mathbf{M} acts as a step function in time at \mathbf{x}_s , so that the body force is also a step function, and (8.26) is directly applicable. The i th excitation coefficient is now

$$\begin{aligned} \int_V {}_i \mathbf{u}^*(\boldsymbol{\xi}) \cdot \mathbf{f}(\boldsymbol{\xi}) dV &= -M_{pq} \int_V {}_i \mathbf{u}_p^*(\boldsymbol{\xi}) \frac{\partial}{\partial \xi_q} \delta(\boldsymbol{\xi} - \mathbf{x}_s) dV(\boldsymbol{\xi}) \\ &= {}_i u_{p,q}^*(\mathbf{x}_s) M_{pq} = {}_i e_{pq}^*(\mathbf{x}_s) M_{pq}, \end{aligned} \quad (8.29)$$

where ${}_i e_{pq}$ is the (pq) strain component in the i th normal mode. To obtain the last equality in (8.29), we used the symmetry $M_{pq} = M_{qp}$. Putting (8.29) into (8.26), we finally obtain the displacement for an arbitrary point source $\mathbf{M}H(t)$ acting at \mathbf{x}_s :

$$\mathbf{u}(\mathbf{x}, t) = \sum_i [{}_i e_{pq}^*(\mathbf{x}_s) M_{pq}] {}_i \mathbf{u}(\mathbf{x}) \frac{1 - \exp(-\omega_i t / 2Q_i) \cos \omega_i t}{\omega_i^2}. \quad (8.30)$$

Thus, once the normal modes ${}_i \mathbf{u}$ of the Earth are known, it is conceptually a simple matter to calculate the response of the Earth to a point source with arbitrary moment tensor.

To find explicit forms for the normal modes, we must be more specific about the Earth model. We shall consider here a nonrotating spherically symmetric Earth in which the density ρ and Lamé parameters λ and μ depend only on the distance r from the center of symmetry. The equations of motion (2.47)–(2.50) for this model can fruitfully be studied by the motion-stress vector approach that we adopted in Chapter 7. In spherical polar

coordinates, the appropriate ansatz for displacement in the mode (l, m, n) is

$$[{}_n U_l(r) \mathbf{R}_l^m(\Delta, \phi) + {}_n V_l(r) \mathbf{S}_l^m(\Delta, \phi) + {}_n W_l(r) \mathbf{T}_l^m(\Delta, \phi)] \exp(-i_n \omega_l t). \quad (8.31)$$

The associated traction working on spherical surfaces $r = \text{constant}$ is

$$[{}_n R_l(r) \mathbf{R}_l^m(\Delta, \phi) + {}_n S_l(r) \mathbf{S}_l^m(\Delta, \phi) + {}_n T_l(r) \mathbf{T}_l^m(\Delta, \phi)] \exp(-i_n \omega_l t) \quad (8.32)$$

and we can write the equations for the radial function in the following separate forms:

$$\frac{d}{dr} \begin{pmatrix} V \\ U \\ S \\ R \end{pmatrix} = \begin{pmatrix} \frac{1}{r} & -\frac{\sqrt{l(l+1)}}{r} & \frac{1}{\mu} & 0 \\ \frac{\lambda\sqrt{l(l+1)}}{r(\lambda+2\mu)} & -\frac{2\lambda}{r(\lambda+2\mu)} & 0 & \frac{1}{\lambda+2\mu} \\ \frac{4l(l+1)\mu(\lambda+\mu)}{r^2(\lambda+2\mu)} - \rho\omega^2 - \frac{2\mu}{r^2} & -\frac{2\mu(3\lambda+2\mu)\sqrt{l(l+1)}}{r^2(\lambda+2\mu)} & -\frac{3}{r} & -\frac{\lambda\sqrt{l(l+1)}}{r(\lambda+2\mu)} \\ -\frac{2\mu(3\lambda+2\mu)\sqrt{l(l+1)}}{r^2(\lambda+2\mu)} & -\rho\omega^2 + \frac{4\mu(3\lambda+2\mu)}{r^2(\lambda+2\mu)} & \frac{\sqrt{l(l+1)}}{r} & -\frac{4\mu}{r(\lambda+2\mu)} \end{pmatrix} \begin{pmatrix} V \\ U \\ S \\ R \end{pmatrix} \quad (8.33)$$

and

$$\frac{d}{dr} \begin{pmatrix} W \\ T \end{pmatrix} = \begin{pmatrix} \frac{1}{r} & \frac{1}{\mu} \\ \frac{\mu(l-1)(l+2)}{r^2} - \rho\omega^2 & -\frac{3}{r} \end{pmatrix} \begin{pmatrix} W \\ T \end{pmatrix}. \quad (8.34)$$

(We have dropped subscripts l and n from the dependent variables and from ω . Note that m does not enter the matrix equations.)

Thus the vibrations of a spherically symmetric Earth without rotation can be separated into two type of modes. One is the spheroidal mode with horizontal wave functions \mathbf{R}_l^m and \mathbf{S}_l^m and radial wavefunctions determined by (8.33). The other is the toroidal or torsional mode with horizontal wavefunction \mathbf{T}_l^m and radial wavefunctions determined by (8.34). It is clear from a comparison of matrices in (8.33) and (7.28) that the spheroidal modes include Rayleigh waves. Comparing (8.34) and (7.24), we see that the toroidal modes include Love waves. Such comparisons require that the horizontal wave number k of surface waves be identified with $\sqrt{l(l+1)}/r$ for free oscillations. We shall present a more detailed comparison of surface waves and free oscillations in the next section.

To find the normal modes, we must solve the eigenvalue–eigenvector problems (8.33) and (8.34) under the boundary conditions that the solutions are regular at $r = 0$ and the tractions vanish at the Earth's surface ($r = r_\oplus$). The numerical method and the Rayleigh–Ritz method described in Chapter 7 can be adapted to solve these problems. One method of handling the condition at $r = 0$ (Takeuchi and Saito, 1972) is to assume that the Earth is uniform in $r < r_1$ and solve the differential equations in powers of r . The power series are then evaluated at $r = r_1$, and numerical integration is initiated from these values and taken upward. For each integer l , there are eigenvalues ${}_n \omega_l (n = 0, 1, 2, \dots)$ that make the stress wavefunctions (R_l, S_l, T_l) all zero at $r = r_\oplus$, and for each ${}_n \omega_l$ there is an eigenfunction for the motion–stress vector. Again we note a degeneracy, in that eigenfrequency and radial eigenfunction are independent of m .

TABLE 8.1
Strain components for a spheroidal mode.

	$m = 0$	$m = \pm 1$	$m = \pm 2$
e_{rr}	$b_0 \frac{dU}{dr}$	0	0
$e_{\Delta\Delta}$	$\frac{b_0}{r} [U - \frac{1}{2} \sqrt{l(l+1)} V]$	0	$\frac{b_0 \sqrt{(l+2)(l-1)}}{4} \frac{V}{r}$
$e_{\phi\phi}$	$e_{\Delta\Delta}$	0	$-e_{\Delta\Delta}$
$2e_{r\Delta}$	0	$\frac{-b_0 m}{2} \left[\frac{\sqrt{l(l+1)}}{r} U + \frac{dV}{dr} - \frac{V}{r} \right]$	0
$2e_{r\phi}$	0	$2ie_{r\Delta}$	0
$2e_{\Delta\phi}$	0	0	$ime_{\Delta\Delta}$

TABLE 8.2
Strain components for a toroidal mode.

	$m = 0$	$m = \pm 1$	$m = \pm 2$
e_{rr}	0	0	0
$e_{\Delta\Delta}$	0	0	$\frac{imb_0}{8} \sqrt{(l+2)(l-1)} \frac{W}{r}$
$e_{\phi\phi}$	0	0	$-e_{\Delta\Delta}$
$2e_{r\Delta}$	0	$\frac{-ib_0}{2} \left[\frac{dW}{dr} - \frac{W}{r} \right]$	0
$2e_{r\phi}$	0	$\frac{b_0 m}{2} \left[\frac{dW}{dr} - \frac{W}{r} \right]$	0
$2e_{\Delta\phi}$	0	0	$\frac{-b_0 \sqrt{(l+2)(l-1)}}{2} \frac{W}{r}$

The asterisk in (8.38) following \dot{M}_{pq} indicates convolution, and (8.38) indicates that the point source is naturally characterized by its moment-rate tensor, $\dot{\mathbf{M}}(t)$.

In this section we have followed the simple and straightforward steps due to Gilbert (1971) and Gilbert and Dziewonski (1975) in deriving the formula for excitation of free oscillations. Earlier, Saito (1967) solved the same problem using a method similar to the one we described for surface-wave excitation in Chapter 7, and he obtained a formula equivalent to (8.30). Figure 8.4 shows a comparison between observed and calculated spectral peaks at several WWSSN stations for a large deep earthquake in Colombia. The continuous lines indicate the observed radial displacement spectrum, and the vertical bars show the theoretical amplitudes of free oscillations calculated by Mendiguren (1973a) using Saito's formula and a focal mechanism determined from the observed P -wave first-motion pattern. Saito's results were used by Mendiguren (1973b) in devising a stacking technique for high-resolution identification of spectral peaks, as described in Box 8.2.

┌

┐

strip in ri09f01

└

┘

FIGURE 9.1

(a) Notation for the density (ρ) and two wave speeds (α , β) in a stack of homogeneous layers. The boundary between layers n and $n + 1$ is at depth z_n , and the thickness of the n th layer is $Th_n = z_n - z_{n-1}$. (b) Ray interpretation for the two main contributions to the generalized P -wave reflection associated with the n th boundary; source and receiver are in layer 1. We have assumed $\alpha_{n+1} > \alpha_n$, so that a head wave (involving horizontal propagation at the top of the $(n + 1)$ th layer) can exist, together with a wide-angle reflection, as shown. Because this generalized reflection is associated with only one interface, it is known as a *primary* reflection. No mode conversions (from P to SV) are shown. In practice, for a P -wave source, it is often true that the total P -wave response at the receiver is given quite accurately by summing such primary reflections, one for each interface (i.e., by ignoring multiple internal reflections and conversions from P to SV and back to P).

where K_0 is a modified Bessel function and

$$\begin{aligned} \text{PRODUCT}(p) = & (\dot{P}\dot{P})_1 \cdot (\dot{P}\dot{P})_2 \cdots (\dot{P}\dot{P})_{n-1} \cdot (\dot{P}\dot{P})_n \\ & \cdot (\dot{P}\dot{P})_{n-1} \cdots (\dot{P}\dot{P})_2 \cdot (\dot{P}\dot{P})_1, \end{aligned} \quad (9.3)$$

$$\begin{aligned} \text{SUM}(p) = & (Th_1 - d_1)\xi_1 + Th_2\xi_2 + \cdots + Th_n\xi_n \\ & + Th_n\xi_n + \cdots + Th_2\xi_2 + (Th_1 - d_2)\xi_1. \end{aligned} \quad (9.4)$$

Here, $\xi_i = \sqrt{\alpha_i^{-2} - p^2}$ with branch cuts chosen by $\text{Re } \xi_i \geq 0$, and $(\dot{P}\dot{P})_{n-1}$ (etc.) is a transmission coefficient for the $(n - 1)$ th boundary. The product in (9.3), involving plane-wave transmission and reflection coefficients, is easily written down with an eye on Figure 9.1b, following the generalized ray across interfaces. (Although our physical

art/ri09f14.eps

FIGURE 9.14

The behavior of T , Δ , and τ as functions of p for a velocity decrease with depth. (a) A low-velocity zone (within which $d\alpha/dr > \alpha/r$ and there are no turning points) is shown shaded, and a shadow within which no rays are received is observed at the surface. (b) The travel-time curve. The upper boundary of the low-velocity zone is the turning point for the ray emerging at point E . Point F has the same ray parameter, but lies on a ray going through the low-velocity zone itself. As ray parameter decreases slightly from its value at F , distance Δ decreases until a caustic is reached at Δ_1 . (c) The values of $\Delta = \Delta(p)$. These show that the further boundary of the shadow is in fact a caustic. (d) Upper and lower boundaries of the low-velocity zone are turning points for rays that differ infinitesimally in their ray parameter. The turning-point radius is therefore a discontinuous function of p . This is also a discontinuity in $\tau(p) = T - p\Delta$ and in the gradient $d\tau/dp = -\Delta(p)$.

so we can rewrite (9.46):

$$Z(p) = \frac{1}{\pi} \int_p^{1/c_0} \frac{X(q) dq}{\sqrt{q^2 - p^2}} + I(p). \quad (9.47)$$

The first term of the right-hand side of the above equation is nothing but the Herglotz–Wiechert formula, and is determined uniquely from the observed travel-time data. The contribution $I(p)$ from the low-velocity layers can be obtained as

$$\begin{aligned} I(p) &= \sum_{i=1}^k \frac{2}{\pi} \int_{z_i}^{\bar{z}_i} dz \int_{p_i}^{1/c(z)} \frac{q dq}{\sqrt{[1/c(z)]^2 - q^2} \sqrt{q^2 - p^2}} \\ &= \sum_{i=1}^k \frac{2}{\pi} \int_{z_i}^{\bar{z}_i} \tan^{-1} \sqrt{\frac{[1/c(z)]^2 - p_i^2}{p_i^2 - p^2}} dz \quad \text{for } p_k > p > p_{k+1}. \end{aligned} \quad (9.48)$$

The above equations (9.47) and (9.48), obtained by Gerver and Markushevitch (1966), represent the extension of the Herglotz–Wiechert formula to include low-velocity layers.

For $p > p_1$, $I(p) = 0$. Therefore, the Herglotz–Wiechert term gives the solution $Z(p)$, which gives the velocity–depth function uniquely for $z < z_1$.

For $p < p_1$, the Herglotz–Wiechert term is determined from the observed travel-time data. However, through the second term $I(p)$, an arbitrary velocity–depth function $v(z)$ may be assigned to the low-velocity layer subject to some constraints described below. Except for the upper boundary of the first low-velocity layer, the boundary depths z_k, \bar{z}_k are also unknown.

The first constraint from observations, on $c(z)$, z_k , and \bar{z}_k , is given by the discontinuity in $\tau(p)$:

$$\Delta \tau_k = 2 \int_{z_k}^{\bar{z}_k} \sqrt{[1/c(z)]^2 - p_k^2} dz. \quad (9.49)$$

The second is, by definition, that the calculated $Z(p)$ should not increase with p . The third is that $Z(p_k + 0)$ and $Z(p_k - 0)$ must agree, respectively, with the depths of the lower and upper boundaries, z_k and \bar{z}_k , of the k th layer. As shown in Figure 9.27, Gerver and Markushevitch gave a “giraffe-like” area in which the plots of all possible solutions $c(z)$ must lie for the case of two low-velocity layers. The upper bound for $c(z)$ corresponds to the Herglotz–Wiechert term. Figure 9.27 also shows the existence of an upper bound for the thickness of the LVZ given earlier by (9.40).

The special methods we have described in this section, for inverting travel-time data, are closely associated with the special properties of the Abel integral equation. These methods are unusual in that a method of *construction* is known for obtaining the inverse. More general methods of inversion, applied to travel times, are described by Johnson and Gilbert (1972).

BOX 9.5 (continued)

Note that B contains the horizontal derivatives present in the Laplacian operator, so that $BY_l^m = -l(l+1)Y_l^m$ for any surface harmonic Y_l^m . The inverse B^{-1} of B has been discussed by Backus (1958): if $g = g(r, \Delta, \phi)$ can be expressed as a sum $g = \sum_{l=1}^{\infty} \sum_{m=-l}^l g_l^m(r) Y_l^m$, then we invert $Bf = g$ to obtain $f = B^{-1}g = -\sum_{l=1}^{\infty} \sum_{m=-l}^l [l(l+1)]^{-1} g_l^m Y_l^m$.

SV-POTENTIAL

For spheroidal motion, $\text{curl}_r \mathbf{u} = 0$, and then $S_r = 0$ and $\nabla \cdot \mathbf{S} = 0$ both follow from (2). Thus $\partial(\sin \Delta S_{\Delta})/\partial \Delta + \partial S_{\phi}/\partial \phi = 0$, which is a condition that there exists a function V such that $S_{\Delta} = (1/\sin \Delta) \partial V/\partial \phi$, $S_{\phi} = -\partial V/\partial \Delta$. Hence

$$\mathbf{S} = \nabla \times (rV, 0, 0) \quad \text{for SV waves.} \quad (5)$$

To construct V , we form $\text{curl}_r \mathbf{S}$ and note that $-r \text{curl}_r \mathbf{S} = BV$, an operator we have already found how to invert. Richards (1974) shows that

$$\nabla^2 V + \frac{\rho\omega^2}{\mu} V = \text{terms of order } \frac{|\mathbf{u}|}{\omega^2}. \quad (6)$$

SH-POTENTIAL

For toroidal motion, $u_r = 0$ and $\nabla \cdot \mathbf{u} = 0$. We can therefore follow the same stages as discussed above for \mathbf{S} , introducing a potential H_0 via $H_0 = -B^{-1}(r \text{curl}_r \mathbf{u})$. To get the canonical form of the wave equation for SH -potential, it is convenient to work with $H = \mu^{1/2} H_0$. Then

$$\mathbf{u} = \mu^{-1/2} \nabla \times (rH, 0, 0) \quad \text{for SH-waves,}$$

and

$$\nabla^2 H + \frac{\rho\omega^2}{\mu} H = \text{terms of order } \frac{|\mathbf{u}|}{\omega}. \quad (7)$$

Equations (9.50a) and (9.50b) are obtained by ignoring small terms in (3)–(7). (All these terms are zero in homogeneous media.)

Following Seckler and Keller (1959) and Friedman (1951), we introduce three particular solutions of the homogeneous equation related to (9.55). Let $f_l(r)$ be that solution for (r, l) which is regular at the central point $r = 0$. For very large values of r , the wave equation becomes roughly $d^2 a/dr^2 = -\omega^2 a/\alpha^2$. By analogy with the solutions $e^{\pm i\omega r/\alpha}$ when α is constant, we expect that two independent solutions of our wave equation can be chosen, one with a phase that increases with r , and another with a phase that decreases. We label these solutions $g_l^{(1)}(r)$ and $g_l^{(2)}(r)$, respectively. In association with the factor $\exp(-i\omega t)$, $g^{(1)}$ is an outgoing wave and $g^{(2)}$ is ingoing. Apart from a normalization, the three solutions are completely defined and we may take

$$a(r, l) = \begin{cases} c_1 g_l^{(1)}(r) & r_s \leq r \\ c_2 f_l(r) & \text{for } 0 \leq r \leq r_s. \end{cases} \quad (9.56)$$



FIGURE 10.1
The origin of coordinates
is taken on a finite fault
surface.

If this error is equal to or greater than a quarter wavelength, $\lambda/4$, a serious error will be introduced in the result of integration. Therefore, the approximation by equation (10.11) is justified only for

$$\frac{1}{2r_0} \left[|\boldsymbol{\xi}|^2 - (\boldsymbol{\xi} \cdot \boldsymbol{\gamma})^2 \right] \ll \frac{\lambda}{4}$$

or, conservatively,

$$L^2 \ll \frac{1}{2} \lambda r_0, \quad (10.12)$$

where L is the maximum of $|\boldsymbol{\xi}|$ on Σ . This is the same as the condition to be satisfied for the region of Fraunhofer diffraction in optics. For comparison, note that the condition we assumed in Chapter 4, in which the whole fault was regarded as a point source, amounted to $L \ll \lambda$, which is a much more restrictive condition on the applicable frequency range than (10.12). Under condition (10.12), we can rewrite the displacement waveform given in equation (10.7) as

$$\Omega(\mathbf{x}, t) = \Omega(\boldsymbol{\gamma}, t) = \iint_{\Sigma} \Delta \dot{u} \left[\boldsymbol{\xi}, t - \frac{r_0 - (\boldsymbol{\xi} \cdot \boldsymbol{\gamma})}{c} \right] d\Sigma. \quad (10.13)$$

Note that the far-field pulse shape depends more directly on $\boldsymbol{\gamma}$ than on \mathbf{x} , since it is position on the focal sphere which governs this pulse shape, and many positions \mathbf{x} have the same value of $\boldsymbol{\gamma}$.

Taking the Fourier transform of the above equation with respect to t , we get

$$\begin{aligned} \Omega(\mathbf{x}, \omega) &= \Omega(\boldsymbol{\gamma}, \omega) = \iint_{\Sigma} \Delta \dot{u}(\boldsymbol{\xi}, \omega) \exp \left\{ \frac{i\omega [r_0 - (\boldsymbol{\xi} \cdot \boldsymbol{\gamma})]}{c} \right\} d\Sigma \\ &= \exp \left(\frac{i\omega r_0}{c} \right) \iint_{\Sigma} \Delta \dot{u}(\boldsymbol{\xi}, \omega) \exp \left[\frac{-i\omega (\boldsymbol{\xi} \cdot \boldsymbol{\gamma})}{c} \right] d\Sigma \end{aligned} \quad (10.14)$$

across a smaller but still significant magnitude range, for events all from the same region, have in some cases reported a different result, namely that stress drop appears to increase monotonically with increasing moment for events below a critical size, becoming constant for events larger than critical (e.g., Shi *et al.*, 1998). Heaton (1990) pointed out numerous earthquakes with fault length much greater than width, for which the rise time was likely to be independent of fault length, resulting in a different scaling law.

An extensive study of source parameters of major earthquakes in and near Japan was made by Kanamori and his colleagues using the Haskell model. The result, as summarized by Kanamori (1973), showed that the amount of slip and the extent of the fault area obtained by the seismic method are in good agreement with those obtained by a static method, using geodetic measurements for earthquakes caused by “brittle elastic” rebound. On the other hand, for earthquakes attributed to “visco-elastic” rebound, the slip and fault area were found to be significantly greater by the static method than by the seismic method, indicating that the seismic event does not totally represent tectonic processes associated with an earthquake. The completion of the Global Positioning Satellite system in the 1990s permits subcentimeter determination of absolute locations of points nearly anywhere on Earth, and Heki *et al.* (1997) made such a measurement of ground displacements at 16 stations in the vicinity of a magnitude 7.8 subduction zone earthquake that occurred on 1994 December 28, off the Sanriku coast of northeastern Japan. During the ensuing 12 months, the displacement of 15 of these sites grew to exceed the displacement that had occurred at the time of the earthquake at these same sites. These authors and DeMets (1997) interpreted the observations as evidence for afterslip, somewhere on the fault plane that ruptured in the main shock, rather than as an effect of viscosity in a lower layer. The motion between tectonic plates is apparently accommodated by a continuum of processes, including slow-rupture earthquakes, aseismic creep, and afterslip, as well as by more conventional earthquakes.

10.1.6 NUCLEATION, SPREADING, AND STOPPING OF RUPTURE

The unidirectional propagation of rupture in Haskell’s source model is an oversimplification of faulting when we look closer at the nucleation of the rupture process. To make the model more realistic, it is desirable to allow rupture to initiate at a point (rather than simultaneously everywhere along a line segment) and then spread out radially (rather than propagate in a single direction), until it covers an arbitrary two-dimensional surface on the fault plane. Far-field waveforms from this type of source model, using a uniform rupture velocity, were first studied by Savage (1966) using equation (10.13).

As shown in Figure 10.6, we shall place the fault in the plane $x_3 = 0$ and assume that rupture propagates from the origin in all directions with uniform velocity v and stops at the perimeter of the fault plane Σ . Initially the rupture front is a circle described by $\rho = vt$, but the final fault will have a perimeter given by $\rho = \rho_b(\phi')$, where (ρ, ϕ') are cylindrical coordinates in the fault plane.

Savage (1966) assumed the displacement discontinuity was a step function in time with final value $\Delta U(\rho, \phi')$. In our notation and using Heaviside step functions, the model can be expressed as

$$\Delta u(\boldsymbol{\xi}, t) = \Delta U(\rho, \phi') H(t - \rho/v) [1 - H(\rho - \rho_b)]. \quad (10.23)$$

strip in ri10f06

FIGURE 10.6

The rupture starts from the origin and spreads in the x_1x_2 -plane with a constant velocity v . Initially, the rupture front is a circle $\rho = vt$, but the final fault plane has a perimeter given by $\rho = \rho_b(\phi')$. P is the observation point, and an element $d\Sigma$ of the fault is shown at (ρ, ϕ') .

Putting this into (10.13), we find

$$\begin{aligned}\Omega(\mathbf{x}, t) &= \iint_{\Sigma} \Delta \dot{u} \left(\boldsymbol{\xi}, t - \frac{r_0 - (\boldsymbol{\xi} \cdot \boldsymbol{\gamma})}{c} \right) d\Sigma(\boldsymbol{\xi}) \\ &= \iint \delta \left(t - \frac{r_0}{c} + \frac{\rho \sin \theta \cos(\phi - \phi')}{c} - \frac{\rho}{v} \right) \Delta U(\rho, \phi') \\ &\quad \times [1 - H(\rho - \rho_b)] \rho d\rho d\phi',\end{aligned}\quad (10.24)$$

where we used the spherical coordinates shown in Figure 10.6 for expressing $(\boldsymbol{\xi} \cdot \boldsymbol{\gamma})$. Since $\int f(x) \delta(ax - b) dx = f(b/a)/a$, the integration with respect to ρ gives

$$\begin{aligned}\int \delta \left(t - \frac{r_0}{c} - \frac{\rho q_c}{v} \right) \Delta U(\rho, \phi') [1 - H(\rho - \rho_b)] \rho d\rho \\ = \left(t - \frac{r_0}{c} \right) \Delta U \left(\frac{t - \frac{r_0}{c}}{q_c/v}, \phi' \right) \frac{v^2}{q_c^2} \quad \text{for } 0 < \frac{t - \frac{r_0}{c}}{q_c/v} < \rho_b \\ = 0 \quad \text{for } \rho_b < \frac{t - \frac{r_0}{c}}{q_c/v},\end{aligned}$$

where $q_c = 1 - (v/c) \sin \theta \cos(\phi - \phi')$ is assumed positive everywhere; in other words, $v < c$ and the rupture is subsonic. [If $v > c$, waves would arrive before r_0/c in the directions (θ, ϕ) for which q_c is negative, because $\Delta U[(t - r_0/c)/(q_c/v), \phi']$ will be nonvanishing for $t < r_0/c$.]

- 10.3 Equation (10.41) amounts to a dynamic boundary condition for tractions on the fault plane. Where do we take this condition into account in setting up a representation of the solution, such as (10.39)? Verify that this representation of the radiated field does indeed have continuity of shear stress across the fault (use results of Problem 10.2).
- 10.4 The opening of a crack may be represented by a displacement discontinuity $[\mathbf{u}]$ that is parallel to \mathbf{v} , the fault normal. Obtain the equivalent body force in an isotropic elastic body, and find the far-field body waves (P and S) in an infinite homogeneous medium (cf. equation (10.6)).
- 10.5 Show that the source spectrum for a faulting episode, derived from the far-field displacement as discussed in Section 10.1.4 in the limit of low frequencies, is flat at the origin ($\omega = 0$). (This result is true, whether the spectrum has a maximum at the origin, or whether there is overshoot.)
- 10.6 Under the assumptions of shear faulting on a plane, and slip everywhere in the same direction, we have seen that the far-field pulse shape is given by (10.13) provided fault length L , wavelength λ , and source–receiver distance r_0 satisfy the constraint $L^2 \ll \frac{1}{2}\lambda r_0$. Far-field pulse shapes for P -waves and S -waves radiate out to every direction on the focal sphere. Suppose that the pulse shape $\Omega(t)$ is radiated as a P -wave in some direction $\boldsymbol{\gamma}^P$.
- Show that it is always possible to find a direction $\boldsymbol{\gamma}^S$ in which this same pulse shape $\Omega(t)$ is radiated as an S -wave (though the arrival time will be different, and note that we are neglecting the effects of different attenuation between P - and S -waves).
 - Show that the relationship between $\boldsymbol{\gamma}^P$ and $\boldsymbol{\gamma}^S$ is similar to Snell's law (5.20) governing the angles i and j of P - and S -waves coupled at a plane interface.
 - Given an S -wave pulse shape observed in direction $\boldsymbol{\gamma}^S$, show that it is *not* always possible to find a direction in which this same pulse shape is observed as a P -wave.
- 10.7 The “finiteness factor” $X^{-1} \sin X$ that appears in equations (10.20)–(10.22) is very simple, because (i) the rupture is unilateral (i.e., it proceeds from one end of the fault to the other); (ii) it has constant rupture velocity; (iii) the fault width W is very small; and (iv) the slip function at each point of the fault plane is the same, apart from a delay due to the time taken for rupture to initiate.
- Suppose that we drop assumptions (i), (ii), and (iii), but retain (iv). Show that the far-field pulse shape is then given by

$$\Omega(\mathbf{x}, \omega) = \Omega_0(\mathbf{x}, \omega) F(\boldsymbol{\gamma}, \omega),$$

where $\Omega_0(\mathbf{x}, \omega)$ is the pulse shape radiated by a point shear dislocation of strength $A \times \Delta u(\omega)$, and the finiteness factor in this more general case is

$$F(\boldsymbol{\gamma}, \omega) = \frac{1}{A} \iint_{\Sigma} \exp i\omega \left[\tau(\boldsymbol{\xi}) - \frac{\boldsymbol{\xi} \cdot \boldsymbol{\gamma}}{c} \right] d\Sigma.$$

FIGURE 11.1
Approximating an arbitrary slip function $\Delta w(x')$ by a superposition of step functions.

strip in ri11f01

For the in-plane problem, a similar relation is found between the shear stress τ_{xy} on the fault plane and slip velocity $\Delta \dot{w}$. Applying the same superposition to equation (10.65), we get

$$\tau_{xy}(x') = -\frac{2\mu\beta^2}{\pi v^3} \left[\sqrt{1 - v^2/\alpha^2} - \frac{(1 - v^2/2\beta^2)^2}{\sqrt{1 - v^2/\beta^2}} \right] \int_{-\infty}^0 \frac{\Delta \dot{w}}{\xi - x'} d\xi. \quad (11.4)$$

In both (11.3) and (11.4), we see that the shear stress on the fault plane is a constant times the Hilbert transform of slip velocity.

A function and its Hilbert transform are very closely related. From Box 5.6, we see that if $g(x)$ is the Hilbert transform of a function $f(x)$, then these two function share a common amplitude spectral density, and their spectral phases differ by $\pi/2$.

Thus the shear stress and the slip velocity on the plane $y = 0$ must share a common amplitude spectral density apart from a constant factor, with a phase difference of $\pi/2$. Furthermore, the slip velocity must be zero outside the crack (because no slip occurs there yet), and the shear stress must be zero inside the crack (assuming no frictional stress for simplicity). In other words, we want to find a pair of functions $f(x)$ and $g(x)$ that satisfy

$$f(x) = 0 \text{ if } x > 0, \quad g(x) = 0 \text{ if } x < 0, \quad \text{and} \quad g(x) = \frac{1}{\pi} \int_{-\infty}^{\infty} \frac{f(\xi)}{\xi - x} d\xi. \quad (11.5)$$

From tables of Hilbert transforms, we find that the following choices of $f(x)$ and $g(x)$ satisfy these three conditions:

$$f(x) = \frac{H(-x)}{\sqrt{-x}} \quad \text{and} \quad g(x) = \frac{-H(x)}{\sqrt{x}}.$$

It is easy to show that they satisfy the integral in equation (11.5) by extending ξ to a complex plane and making a branch cut along the negative real axis (Fig. 11.2). The integral along AO will be equal to the one along OB because of the opposite signs of $\sqrt{-\xi}$ on the two paths. For $x > 0$, the residue evaluation of $\xi = x$ gives $g(x) = 1/\sqrt{x}$, and for $x < 0$ the integral vanishes because the pole is outside the contour.

Thus we find for our mechanics problem that the boundary conditions for a moving crack are satisfied by a square-root singularity in stress ahead of the crack tip, and another square-root singularity in slip velocity behind the crack tip. The square-root singularity in stress is well known for a static crack.



strip in ri11f08

FIGURE 11.8

There is a pole at q_{uv} near the Cagniard path for evaluating (11.31). [From Richards, 1976a.]

out to be a second-order pole, denoted by q_{uv} , and is due to the moving nature of the source. It is necessary to pick up residues in converting to the Cagniard path, giving the form

$$\begin{aligned} \mathbf{u}^P(\mathbf{x}, s) = & \frac{1}{s^2} \int_0^\infty dw \int_0^\infty dt \mathbf{F}(q(t), w, \phi) e^{-st} \frac{dq}{dt} \\ & + \int_0^\infty dw \mathbf{R}(q_{uv}, w, \phi, s) e^{-st} (q_{uv}, w, \theta), \end{aligned} \quad (11.32)$$

From the first term on the right-hand side here, one can invert to the time domain in the usual fashion (i.e., by reversing the order of integration and recognizing the result as a forward Laplace transform), obtaining a single integral over w . The second term on the **right-hand side of (11.32)** is already in the form suitable for recognition as the Laplace transform of a function of time. This term therefore results in an algebraic closed-form expression. This overall method, an algebraic expression resulting from an integral of residues, was first developed by Gakenheimer and Miklowitz (1969) for solving Lamb's problem with a moving source.

As usual for Cagniard inversion of three-dimensional problems (see Section 6.5), the complete seismogram can be calculated only numerically, an integration being necessary for each point in the time series. Figure 11.9 shows theoretical record sections for x_1 - and x_3 -components of acceleration near a left-lateral strike-slip fault. The coordinates for the four stations are (1, 1.5, 0.5), (4, 1.5, 0.5), (7, 1.5, 0.5), and (10, 1.5, 0.5). The density of the medium is 2.7 gm/cm³, the P -wave velocity is 5.2 km/s, and the S -wave velocity is 3 km/s. The rupture speed in the x_1 -direction is 90% of the Rayleigh-wave velocity, and that in the x_2 -direction is 90% of the S -wave velocity. We see, in this case, small P -waves, sharp step-like S -waves arriving from the nucleation point, and large acceleration associated with the passage of the crack tip. The amplitude of waves from the nucleation point decreases with distance, whereas the acceleration associated with passage of the crack tip increases because the stress-intensity factor increases with increasing crack length.

The corresponding displacement records are shown in Figure 11.10. As discussed in Section 11.1.1, the transverse component shows a step-like waveform rather than a



strip in ri11f12

FIGURE 11.12
Grid-point assignment for each
of nine stress/particle-velocity
components.



where λ , μ are the Lamé constants and ρ is the density. We have to solve these equations subject to the following boundary conditions on $z = 0$:

$$\begin{aligned}\Sigma_{rz} = -\Sigma_{\phi z} = -p_0 & \quad \text{for } r < \min(vt, r_c), \\ \dot{u} = \dot{v} = 0 & \quad \text{for } r > \min(vt, r_c), \text{ and} \\ \Sigma_{zz} = 0 & \quad \text{for all } r.\end{aligned}$$

The slip components Δu_1 and Δu_2 in the original coordinates can be written in terms of u and v at $z = 0$:

$$\Delta u_1 = 2u \cos^2 \phi - 2v \sin^2 \phi, \quad \Delta u_2 = (u + v) \sin 2\phi.$$

In the case of self-similar cracks studied in the preceding section, Δu_2 vanishes. In the present case Δu_2 does not necessarily vanish but is found to be practically negligible; i.e., $u \sim -v$, so that

$$\Delta u_1 = 2u = -2v. \quad (11.38)$$

Interestingly, Δu_1 is independent of ϕ .

Madariaga (1976) solved the above problem by the finite-difference method using a so-called staggered grid in which the velocities are defined at discrete times $k \Delta t$ and the stresses at times $(k + \frac{1}{2})\Delta t$, for integer values of k , where Δt is the time-grid interval. The spatial grid-point assignment for each of the nine stress-particle velocity components is shown in Figure 11.12.

Figure 11.13 shows the slip function $\Delta u(r, t) = u(r, +0, t) - u(r, -0, t)$ at several points on the crack. The rupture starts at $t = 0$ and expands with velocity 0.9β , where β is the shear velocity. The slip is measured with $p_0 r_c / \mu$ as the unit. The time t and radial distance r' are normalized to r_c / α and r_c , respectively, where α is the P -velocity. The slip function in time is shown at the center ($r = 0$) and at four other points at intervals of $0.2 r_c$. At each position for which the slip history is shown, an arrow indicates the time of arrival of P -waves, originating from the perimeter of the crack at the instant the rupture

re-leveled to maintain the bubble position. Using this feedback as the output signal, Harrison was able to measure the M_2 tide to about 0.5% after 3 months of observation. However, short-base tiltmeters are inherently susceptible to very local site effects, which are hard to quantify. If nearby rock units are heterogeneous, then an applied overall strain can cause local tilting, which partly explains why closely spaced short-baseline tiltmeters do not always give the same signal.

12.2 Frequency and Dynamic Range of Seismic Signals and Noise

Most of the signals studied in seismology are transient, i.e., they have in practice a finite duration, such as seismograms from explosions and earthquakes. For such a transient signal $f(t)$, the Fourier transform $f(\omega)$ exists with the definition

$$f(\omega) = \int_{-\infty}^{\infty} f(t)e^{i\omega t} dt, \quad \text{and} \quad f(t) = \int_{-\infty}^{\infty} f(\omega)e^{-i\omega t} \frac{d\omega}{2\pi}, \quad (12.21)$$

in which t is the time and ω is the angular frequency. We shall define the *amplitude spectral density* as the absolute value of $f(\omega)$, and the *phase-delay spectrum* $\phi(\omega)$, by

$$f(\omega) = |f(\omega)|e^{i\phi(\omega)}. \quad (12.22)$$

Our reason for calling ϕ the phase delay is given in Box 5.5. Since $f(t)$ is real,

$$f^*(\omega) = f(-\omega), \quad |f(\omega)| = |f(-\omega)|, \quad \text{and} \quad \phi(\omega) = -\phi(-\omega), \quad (12.23)$$

where the asterisk indicates the complex conjugate.

The unit of $|f(\omega)|$ is the unit of $f(t)$ divided by the unit of frequency ($\omega/2\pi$). For example, if $f(t)$ represents the ground displacement in cm, then the unit of $|f(\omega)|$ is cm per Hz—which explains why $|f(\omega)|$ is called the amplitude spectral *density* (though the abbreviation “amplitude spectrum” is common). The most commonly used units of $\phi(\omega)$ are the radian or the circle (i.e., 2π radians).

There are three other distinct types of signal for which the ordinary Fourier transform does not exist. One is the superposition of sinusoidal oscillations with frequencies ω_n , such as the tidal Earth-strain caused by the gravitational attraction of the Sun and the Moon. For this, we define amplitude A_n and phase delay ϕ_n in the following manner:

$$f(t) = \sum_n A_n \exp(-i\omega_n t + i\phi_n), \quad (12.24)$$

where A_n has the same physical dimension as $f(t)$.

Another type of signal we shall consider is the stationary stochastic process, such as ambient seismic ground noise caused by the atmosphere, the oceans, some volcanic processes, industrial activities, and traffic. These signals cannot be expressed either by (12.21) or by (12.24). We first introduce the *autocorrelation function* $P(\tau)$, defined as

$$P(\tau) = \langle f(t)f(t + \tau) \rangle, \quad (12.25)$$

This gives a ground acceleration equivalent to the Brownian motion of the pendulum. Using $Q^{-1} = 2\varepsilon/\omega_s$, where $2\pi/\omega_s = T_s$ is the undamped pendulum period, (12.39) is rewritten as

$$\frac{\langle \alpha^2(t) \rangle}{\Delta f} = \frac{8\pi kT}{MQT_s}. \quad (12.40)$$

Thus the instrumental acceleration-noise power-density is inversely proportional to the product of mass, instrument Q , and pendulum period.

For comparison with the ground-noise spectra given in Figure 12.12, it is interesting to note that the Low Noise Model ground-noise spectrum is approximately flat in acceleration for frequencies in the range 0.002 to 0.03 Hz, and also for frequencies greater than about 1.5 Hz. In order to estimate the instrument parameters required for the thermal noise to be kept below the ground noise, we can therefore fit (12.40) to the observed LNM ground noise spectra, shown in Figure 12.12b, at long periods and short periods separately. From the figure, we would want

$$\begin{aligned} \frac{8\pi kT}{MQT_s} &< 10^{-17}(\text{m/s})^2/\text{Hz} && \text{at frequencies below 0.03 Hz,} \\ &< 10^{-19}(\text{m/s})^2/\text{Hz} && \text{at frequencies above 1.5 Hz.} \end{aligned}$$

Putting $kT \sim 4 \times 10^{-14}$ erg, we therefore find that the requirement for thermal noise to be below the ground noise is given approximately by

$$MQT_s > 1 \text{ kg-s} \quad \text{for long periods} \quad (12.41)$$

and

$$MQT_s > 0.01 \text{ kg-s} \quad \text{for short periods.} \quad (12.42)$$

The traditional long-period seismograph has about a 10-kg mass and a period of 15–30 s, easily satisfying (12.41) with near-critical damping ($Q = \frac{1}{2}$). One of the first instruments to satisfy the long-period requirement (12.41) with much smaller mass was an accelerometer described by Block and Moore (1970). This instrument had M about 10 grams and a relatively short period of 1 s, and it achieved low thermal noise by making the pendulum Q high (200) and using capacitive sensing and electrostatic feedback—techniques we discuss further in Section 12.3.6.

Many simple short-period seismometers still in common use have pendulum periods of 0.1 to 1 s. The mass required to overcome the thermal noise is then only 10 to 100 grams. The pendulum mass traditionally used in the short-period sensor of the Worldwide Standardized Seismographic System is much larger. The sensing device of these instruments (a moving coil in a magnet gap) requires a larger pendulum mass for greater signal power, as shown in the next section.

12.3.2 ELECTROMAGNETIC VELOCITY SENSOR

The motion of a pendulum relative to the seismometer frame was for decades measured most commonly in seismology by the electromagnetic velocity sensor shown schematically

- Mendiguren, J. Identification of free oscillation spectral peaks for 1970 July 31, Colombian deep shock using the excitation criterion. *Geophysical Journal of the Royal Astronomical Society*, **33**, 281–321, 1973a.
- . High resolution spectroscopy of the Earth's free oscillations, knowing the earthquake source mechanism. *Science*, **179**, 179–180, 1973b.
- Menke, W. *Geophysical Data Analysis: Discrete Inverse Theory*, New York: Academic Press, 1984.
- Michelson, A. A., and H. G. Gale. The rigidity of the Earth. *Astrophysical Journal*, **50**, 330–345, 1919.
- Mikumo, T., and T. Miyatake. Dynamic rupture process on a three-dimensional fault with non-uniform frictions and near-field seismic waves. *Geophysical Journal of the Royal Astronomical Society*, **54**, 417–438, 1978.
- Minakami, T. Seismology of volcanoes in Japan. In *Physical Volcanology*, edited by L. Civetta, P. Jaspardini, G. Luongo, and A. Rapolla. Amsterdam: Elsevier, 1974.
- Mitra, M. Surface displacement produced by an underground fracture. *Geophysical Journal of the Royal Astronomical Society*, **31**, 204–213, 1966.
- Molnar, P., K. H. Jacob, and K. McCamy. Implications of Archaibeau's earthquake source theory for slip on faults. *Bulletin of the Seismological Society of America*, **63**, 101–104, 1973.
- Molnar, P., and J. Oliver. Lateral variations of attenuation in the upper mantle and discontinuities in the lithosphere. *Journal of Geophysical Research*, **74**, 2648–2682, 1969.
- Molnar, P., B. E. Tucker, and J. N. Brune. Corner frequencies of *P* and *S* waves and models of earthquake sources. *Bulletin of the Seismological Society of America*, **63**, 2091–2104, 1973.
- Mora, P., and D. Place. Simulation of the frictional stick-slip instability. *Pure and Applied Geophysics*, **143**, 61–87, 1994.
- Müller, G. Amplitude studies of core phases. *Journal of Geophysical Research*, **78**, 3469–3490, 1973a.
- . Correction. *Journal of Geophysical Research*, **82**, 2541–2542, 1977.
- . Seismic moment and long-period radiation of underground nuclear explosions. *Bulletin of the Seismological Society of America*, **63**, 847–857, 1973b.
- . Volume change of seismic sources from moment tensors. *Bulletin of the Seismological Society of America*, **91**, 880–884, 2001.
- Müller, G., and R. Kind. Observed and computed seismogram sections for the whole Earth. *Geophysical Journal of the Royal Astronomical Society*, **44**, 699–716, 1976.
- Musgrave, M. J. P. *Crystal Acoustics*. San Francisco: Holden-Day, 1970.
- Nafe, J. E. Reflection and transmission coefficients at a solid-solid interface of high velocity contrast. *Bulletin of the Seismological Society of America*, **47**, 205–219, 1957.
- Nakanishi, K., F. Schwab, and L. Knopoff. Generation of complete theoretical seismograms for *SH-I*. *Geophysical Journal of the Royal Astronomical Society*, **48**, 525–530, 1977.